JCI insight

RESEARCH ARTICLE

Molecular mechanisms of IL-33–mediated stromal interactions in cancer metastasis

Patrik Andersson,[1] Yunlong Yang,[1] Kayoko Hosaka,[1] Yin Zhang,[1] Carina Fischer,[1] Harald Braun,[2,3] Shuzhen Liu,[4] Guohua Yu,[4] Shihai Liu,[5] Rudi Beyaert,[2,3] Mayland Chang,[6] Qi Li,[7] and Yihai Cao[1]

[1]Department of Microbiology, Tumor and Cell Biology, Karolinska Institutet, Stockholm, Sweden. [2]Department of Biomedical Molecular Biology, Ghent University, Ghent, Belgium. [3]Unit of Molecular Signal Transduction in Inflammation, Center for Inflammation Research, VIB Ghent, Belgium. [4]Clinical Oncology Department, Weifang People's Hospital, Kuiwen District, Weifang, Shandong, China. [5]Central Research Laboratory, The Affiliated Hospital of Qingdao University, Qingdao, China. [6]Department of Chemistry and Biochemistry, University of Notre Dame, Notre Dame, Indiana, USA. [7]Department of Medical Oncology and Cancer Institute, Shuguang Hospital Shanghai University of Traditional Chinese Medicine, Shanghai, China.

Molecular mechanisms underlying the cancer stroma in metastasis need further exploration. Here, we discovered that cancer-associated fibroblasts (CAFs) produced high levels of IL-33 that acted on tumor-associated macrophages (TAMs), causing them to undergo the M1 to M2 transition. Genomic profiling of metastasis-related genes in the IL-33–stimulated TAMs showed a >200-fold increase of MMP9. Signaling analysis demonstrated the IL-33-ST2-NF-κB-MMP9-laminin pathway that governed tumor stroma–mediated metastasis. In mouse and human fibroblast-rich pancreatic cancers, genetic deletion of IL-33, ST2, or MMP9 markedly blocked metastasis. Pharmacological inhibition of NF-κB and MMP9 also blocked cancer metastasis. Deletion of IL-33, ST2, or MMP9 restored laminin, a key basement membrane component associated with tumor microvessels. Together, our data provide mechanistic insights on the IL-33-NF-κB-MMP9-laminin axis that mediates the CAF-TAM–committed cancer metastasis. Thus, targeting the CAF-TAM-vessel axis provides an outstanding therapeutic opportunity for cancer treatment.

Introduction

Malignant cells live in a complex environment where multiple host cells (collectively called tumor stroma) relentlessly communicate with each other (1). In the tumor microenvironment (TME), cancer cells often instruct stromal cells, including cancer-associated fibroblasts (CAFs), tumor-associated macrophages (TAMs), vascular cells, adipocytes, and even immune cells, in support of their growth and spreading. In most solid cancers, the stroma component dominates the entire tumor tissue (2). For example, the stromal component may account for more than 90% of the total tissue volume of pancreatic cancer (3, 4). Moreover, the composition of tumor stroma is correlated with poor survival of cancer patients (5).

Metastasis is responsible for most cancer death and consists of multistep distinct processes (6, 7). Dissemination of cancer cells from the primary site is the initial early event of cancer metastasis. It appears that malignant cells, without assistance from other cell types, such as stromal fibroblasts, macrophages, and vascular cells, are not sufficiently capable to accomplish the dissemination process. For example, malignant cells from an invasive cancer alone are unable to disseminate in the absence of TAMs (8–10). For intravasation into the blood vessels, malignant cells need to decompose the basement membrane (BM) and transmigrate across the vessel wall. It is known that CAFs and TAMs play important roles in promoting cancer cell dissemination (2, 8, 11). However, molecular mechanisms of the collaborative efforts between these nonmalignant cells in cancer metastasis remain largely unknown. It is still unclear how tumor cells hijack macrophages to transmigrate through the vessel wall.

Cellular multiplicity and heterogeneity determine the existence of multiple signaling pathways in TME (12, 13). It is known that tumor cells produce various factors and cytokines to induce fibrosis, inflammation, and angiogenesis (12). However, less is known about the coordination of these various processes in cancer invasion and metastasis. In particular, the molecular identity of ultimate effectors for initiating cancer metastasis is unknown. While most studies on cancer metastasis focus on the interaction between malignant cells and host cellular components, complex cellular and molecular interactions between various TME stromal

Conflict of interest The authors have declared that no conflict of interest exists.

Submitted: May 22, 2018
Accepted: September 11, 2018
Published: October 18, 2018

Reference information:
JCI Insight. 2018;3(20):e122375.
https://doi.org/10.1172/jci.insight.122375.

compartments are largely overlooked. In this study, we showed that CAFs rather than tumor cells per se instruct inflammatory cells for cancer invasion. We uncover a sophisticated mechanism in which sequential events occur involving the intimate coordination among cancer cells, CAFs, TAMs, and vessels in metastasis. At the molecular level, IL-33-ST2-NF-κB-MMP9-laminin signaling mediates the cross-communications among various cellular components for cancer metastasis. Thus, our results define a metastatic signaling pathway and provide an exciting opportunity for cancer therapy.

Results

PDGFRβ$^+$ stromal cell–derived IL-33 commits the M2 macrophage polarization. CAFs constitute a major part of the entire tumor volume in certain tumors. For example, in pancreatic ductal adenocarcinoma (PDAC), the tumor stromal component mainly consisting of CAFs may occupy approximately 90% of the total tumor volume (4). We recently showed that PDGFRβ$^+$ cells in different tumors produce high levels of IL-33 (14), a member of the IL-1 family that potently drives production of Th2-associated cytokines (15–17). However, the exact cellular source of IL-33 in tumor tissues remains to be identified. We screened a broad spectrum of in vivo tumor tissues for IL-33 production. These included murine B16 melanoma, CT26 colon cancer, E0771 mammary cancer, LLC lung cancer, MC38 colon cancer, Panc02 pancreatic cancer, and T241 fibrosarcoma. Compared with other cancer types, Panc02 pancreatic cancer expressed an exceptionally high level of IL-33 (Figure 1A). To define cell types in the Panc02 tumor tissue that were responsible for IL-33 production, we isolated various cellular fractions. Interestingly, Panc02 tumor cells per se produced a very low level of IL-33 protein (Figure 1B). Similarly, F4/80$^+$ inflammatory cells also produce a negligible level of IL-33. Most IL-33 proteins were synthesized in the nonmalignant and F4/80$^-$ fractions (Figure 1B). Further cell type analysis showed that the PDGFRβ$^+$ population in Panc02 tumors was responsible for producing IL-33 (Figure 1B). These data specify that the PDGFRβ$^+$ cell population consisting of CAFs and perivascular cells is responsible for producing IL-33 in TME.

Cellular composition analysis of Panc02 tumors showed a high proportion of the Masson's trichrome$^+$ fibrotic component (Figure 1C). Consistently, IL-33–producing Panc02, but not IL-33$^-$ LLC, tumors exhibited robust PDGFRβ positivity, which was localized in stromal cells (Figure 1C). Along with the high content of PDGFRβ$^+$ fibrotic cells, Panc02 tumors were also infiltrated with an extraordinary high number of Iba1$^+$ TAMs (Figure 1D). Moreover, an exceptionally high number of CD206$^+$ TAMs was detected, suggesting the M2 polarization occurred in this tumor (Figure 1D). To study the causational link between IL-33 and the M2 TAM polarization, we performed genome-wide expression profiling of IL-33–stimulated and non-stimulated macrophages. IL-33–stimulated macrophages showed marked upregulation of M2-related genes, including *Arg1*, *Ccr3*, *Cd163*, *Cdh1*, *F13a1*, *Hmox1*, *Il1r2*, *Mrc1*, *Pdcdl1g2*, *Serpinb2*, and *Stab1* (Figure 1E). Quantitative validation analysis further confirmed that IL-33–stimulated macrophages expressed increased levels of *Cd206*, *Pdl2*, and *Ccr3* (Figure 1F) and significantly downregulated the M1 markers *Cxcl9* and *Cxcl11* (Supplemental Figure 1A; supplemental material available online with this article; https://doi.org/10.1172/jci.insight.122375DS1). Consistently, increased levels of M2 markers in IL-33–stimulated macrophages were further validated by FACS analysis (Figure 1G).

Knowing the IL-33–committed M2 polarization, we further investigated the M2 polarization in Panc02 tumors grown in ST2-deficient (ST2 KO) mice. Deletion of ST2 receptor in mice resulted in substantial loss of M2 macrophage markers (Supplemental Figure 1B). Downregulation of M2-related markers in F4/80$^+$ Panc02 TAMs was further validated by quantitative PCR (qPCR) analysis (Supplemental Figure 1C). Together, these data demonstrate that PDGFRβ$^+$ stromal fibroblasts and perivascular cells are the major cellular source of IL-33 production, which commits TAMs toward M2 polarization through its ST2 receptor (Figure 1H). Expression of the ST2 receptor has been described in one of our previous studies (14). It is highly likely that IL-33 recruits ST2$^+$ monocytes and converts them into M2 TAMs.

ST2-dependent mechanism of MMP9 upregulation in macrophages. M2 TAMs are known to promote cancer invasion and metastasis (8, 10). However, detailed molecular mechanisms underlying M2 macrophage–mediated metastasis need to be elucidated. To gain mechanistic insights, we analyzed cancer metastasis–related gene expression profiling in IL-33–stimulated macrophages. Several MMPs, including *Mmp12*, *Mmp8*, *Mmp9*, *Mmp13*, *Mmp7*, and *Mmp27*, were markedly increased (Figure 2A). These profiling data suggested to us that MMPs might play important roles in mediating IL-33–promoted metastasis. Elevated levels of MMPs were further validated by qPCR analysis. Surprisingly, a nearly 100-fold increase of *Mmp9* mRNA was detected in macrophages after 24 hours of stimulation with IL-33, although other MMPs were

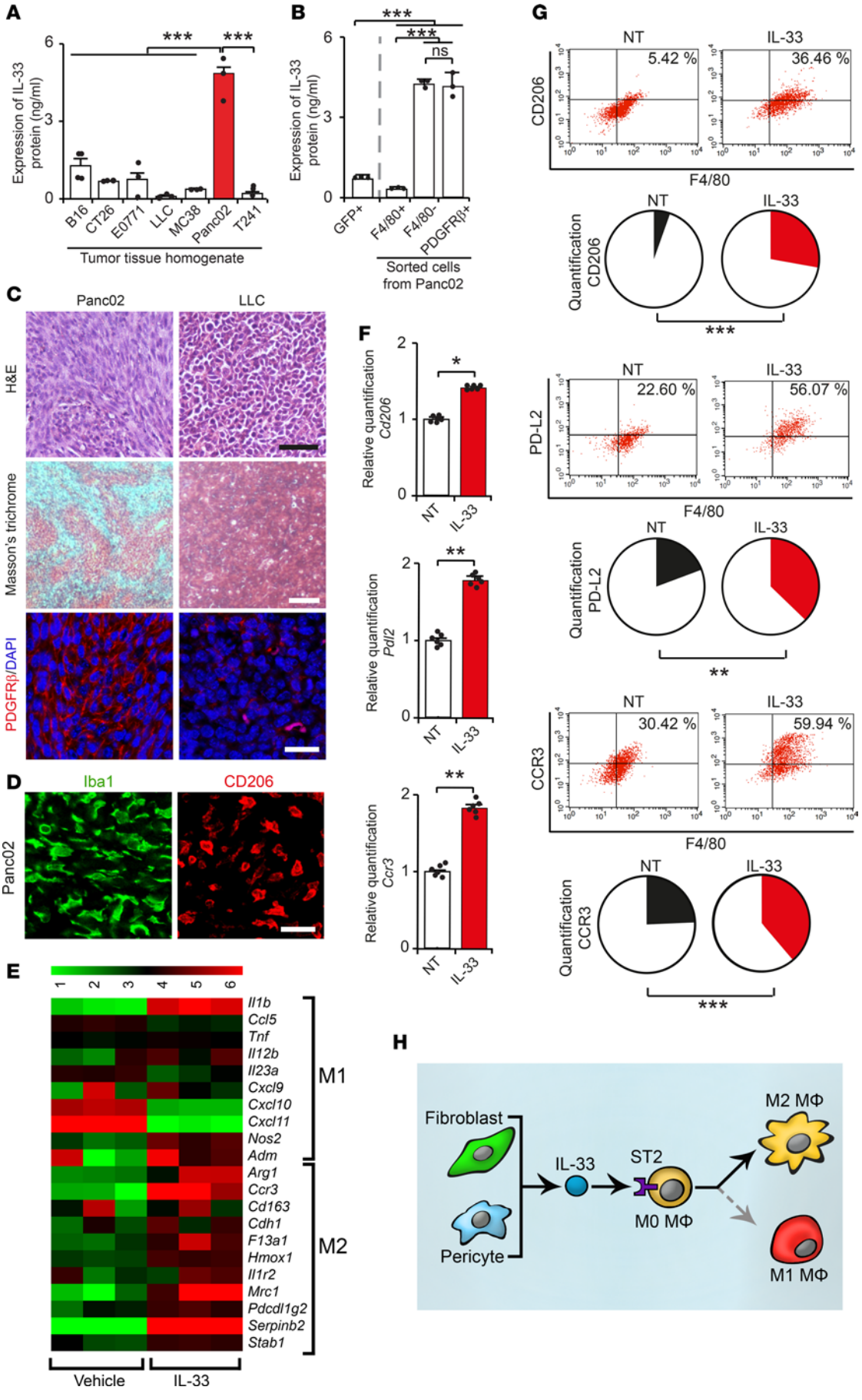
A
Expression of IL-33 protein (ng/ml)
***
***
B16
CT26
E0771
LLC
MC38
Panc02
T241
Tumor tissue homogenate
B
Expression of IL-33 protein (ng/ml)
***
***
ns
GFP+
F4/80+
F4/80-
PDGFRβ+
Sorted cells from Panc02
C
Panc02
LLC
H&E
Masson's trichrome
PDGFRβ/DAPI
D
Iba1
CD206
Panc02
E
1 2 3 4 5 6
Il1b
Ccl5
Tnf
Il12b
Il23a
Cxcl9
Cxcl10
Cxcl11
Nos2
Adm
Arg1
Ccr3
Cd163
Cdh1
F13a1
Hmox1
Il1r2
Mrc1
Pdcdl1g2
Serpinb2
Stab1
M1
M2
Vehicle
IL-33
F
Relative quantification Cd206
*
Relative quantification Pdl2
**
Relative quantification Ccr3
**
NT
IL-33
G
NT
IL-33
5.42 %
36.46 %
CD206
F4/80
Quantification CD206
***
22.60 %
56.07 %
PD-L2
Quantification PD-L2
**
30.42 %
59.94 %
CCR3
Quantification CCR3
***
H
Fibroblast
Pericyte
IL-33
ST2
M0 MΦ
M2 MΦ
M1 MΦ

Figure 1. Noninflammatory stromal cell–derived IL-33 promotes tumor M2 TAM polarization. (**A**) IL-33 protein levels in various tumor tissues (n = 3–4 samples per group). (**B**) IL-33 protein levels of tumor cell (GFP$^+$), F4/80$^+$ inflammatory cell, and F4/80$^-$ or PDGFRβ$^+$ stromal cell fractions isolated from Panc02 tumors (n = 3 samples per group). (**C**) Staining of Panc02 and LLC tumor tissues. H&E (scale bar: 50 μm); Masson's trichrome (light blue, fibrotic components; scale bar: 100 μm); and PDGFRβ$^+$ (red) cells and DAPI$^+$ (blue) nuclei (scale bar: 20 μm). (**D**) Iba1$^+$ (green) and CD206$^+$ (red) macrophages in Panc02 tumors (scale bar: 20 μm). (**E**) Heatmap of subsets of M1- and M2-related genes by genome-wide expression profiling of IL-33–stimulated macrophages (n = 3 samples per group). (**F**) qPCR quantification of *Cd206*, *Pdl2*, and *Ccr3* mRNA expression levels of IL-33–stimulated macrophages (n = 6 samples per group). NT, nontreated. (**G**) FACS analysis of F4/80$^+$/CD206$^+$, F4/80$^+$/PD-L2$^+$, and F4/80$^+$/CCR3$^+$ cell populations in IL-33–stimulated macrophages (n = 6 samples per group). (**H**) Schematic showing that pericyte/stromal fibroblast–derived IL-33 stimulates M2 macrophage polarization through a ST2-dependent mechanism. Mean ± SEM. $^*P < 0.05$; $^{**}P < 0.01$; $^{***}P < 0.001$, Student's t test.

also increased at moderate levels (Figure 2B). Interestingly, prolonged IL-33 stimulation further augmented MMP9 production greater than 230-fold (Figure 2C). Importantly, a soluble ST2 (sST2) receptor (IL-33 trap) (18) inhibited *Mmp9* production in a dose-dependent manner (Figure 2C), linking the IL-33-ST2 signaling to MMP9. In agreement with elevated mRNA levels, IL-33 also markedly increased MMP9 protein activity (Figure 2D). In addition to MMP9 upregulation, several tissue inhibitors of metalloproteinases (TIMPs), including *Timp2*, *Timp3*, and *Timp4*, were downregulated (Supplemental Figure 2A).

We next isolated F4/80$^+$ TAMs and F4/80$^-$ cells from Panc02 tumors grown in WT and ST2 KO mice (17) for detection of MMP9 production. *Mmp9* mRNA expression in F4/80$^+$ TAMs was markedly inhibited in ST2 KO mice, whereas deletion of ST2 in mice had no effect on Mmp9 expression in the F4/80$^-$ fraction (Figure 2E and Supplemental Figure 2B). Consistent with inhibition of MMP9 production, the IL-33 trap also led to reduced MMP9 enzymatic activity, as detected by a zymographic analysis using gelatin as a substrate (Figure 2F). These results show that IL-33 promotes MMP9 production and activity through the ST2 receptor in macrophages.

NF-κB–dependent mechanism of IL-33–induced MMP9 production. To define signaling pathways mediating IL-33–induced MMP9 production, we analyzed activation of intracellular signaling components. Among analyzed signaling molecules, IκBα became highly phosphorylated upon IL-33 stimulation in macrophages (Figure 3A). Similarly, Erk and p38 were also markedly activated by IL-33. To pinpoint the functional link between these signaling molecules and MMP9 production, we employed pharmacological approaches using inhibitors specifically targeting each of these signaling components. Interestingly, withaferin A, an upstream IKKβ inhibitor that blocks NF-κB signaling (19), sufficiently inhibited IL-33–induced *Mmp9* production (Figure 3B). Conversely, an Erk inhibitor U0126 and a p38 inhibitor SB203580 had no effect on *Mmp9* production. An IL-33 trap completely blocked IκBα activation in IL-33–stimulated macrophages (Figure 3C). Protein interaction and pathway analyses supported that IL-33 triggered the signaling pathway for NF-κB activation (Figure 3D). These findings demonstrate that activation of NF-κB is essential for upregulation of MMP9 expression.

We have noticed that mRNA and protein expression levels of NF-κB in IL-33–stimulated and nonstimulated macrophages remained unchanged (Supplemental Figure 3, A and B). As a transcription factor, nuclear translocation of NF-κB is essential for regulating its gene targets (20). We therefore studied NF-κB nuclear translocation in IL-33–stimulated macrophages. Interestingly, in nonstimulated macrophages, NF-κB was largely distributed in the perinuclear area and little positivity was found in cell nuclei (Figure 3E). However, IL-33 stimulation significantly induced a time-dependent NF-κB nuclear translocation (Figure 3E). After 60-minute stimulation, virtually all NF-κB molecules were localized in cell nuclei, indicating a functional effect of IL-33 on NF-κB nuclear translocation. Notably, withaferin A effectively inhibited NF-κB nuclear translocation in a dose-dependent manner (Figure 3F). Along with inhibiting NF-κB nuclear translocation and activation, withaferin A potently blocked IL-33–induced *Mmp9* mRNA production and enzymatic activity (Figure 3, G and H).

NF-κB targets MMP9 promoter for transcription activation. To provide further mechanistic insights on NF-κB–regulated MMP9 expression, we utilized an *Mmp9* promoter-luciferase reporter construct. There are 5 NF-κB–binding sites in the proximal region of the mouse *Mmp9* promoter (Figure 3I), indicating that *Mmp9* is the targeted gene for NF-κB transcriptional activation. Similarly, the human *Mmp9* promoter contains 4 NF-κB–binding sites. IL-33 stimulation of the *Mmp9* promoter-luciferase-transfected macrophages resulted in an approximate 5-fold increase of luciferase activity (Figure 3J). These data indicate that IL-33 induces MMP9 expression through transcription activation on the *Mmp9* promoter.

To link transcription activation of IL-33–induced MMP9 expression to NF-κB, withaferin A was added to the transfected cells in the presence and absence of IL-33. Intriguingly, withaferin A at 2 concentrations markedly blocked IL-33–induced *Mmp9* transcripts (Figure 3J). At the concentration of 0.4 μM, withaferin

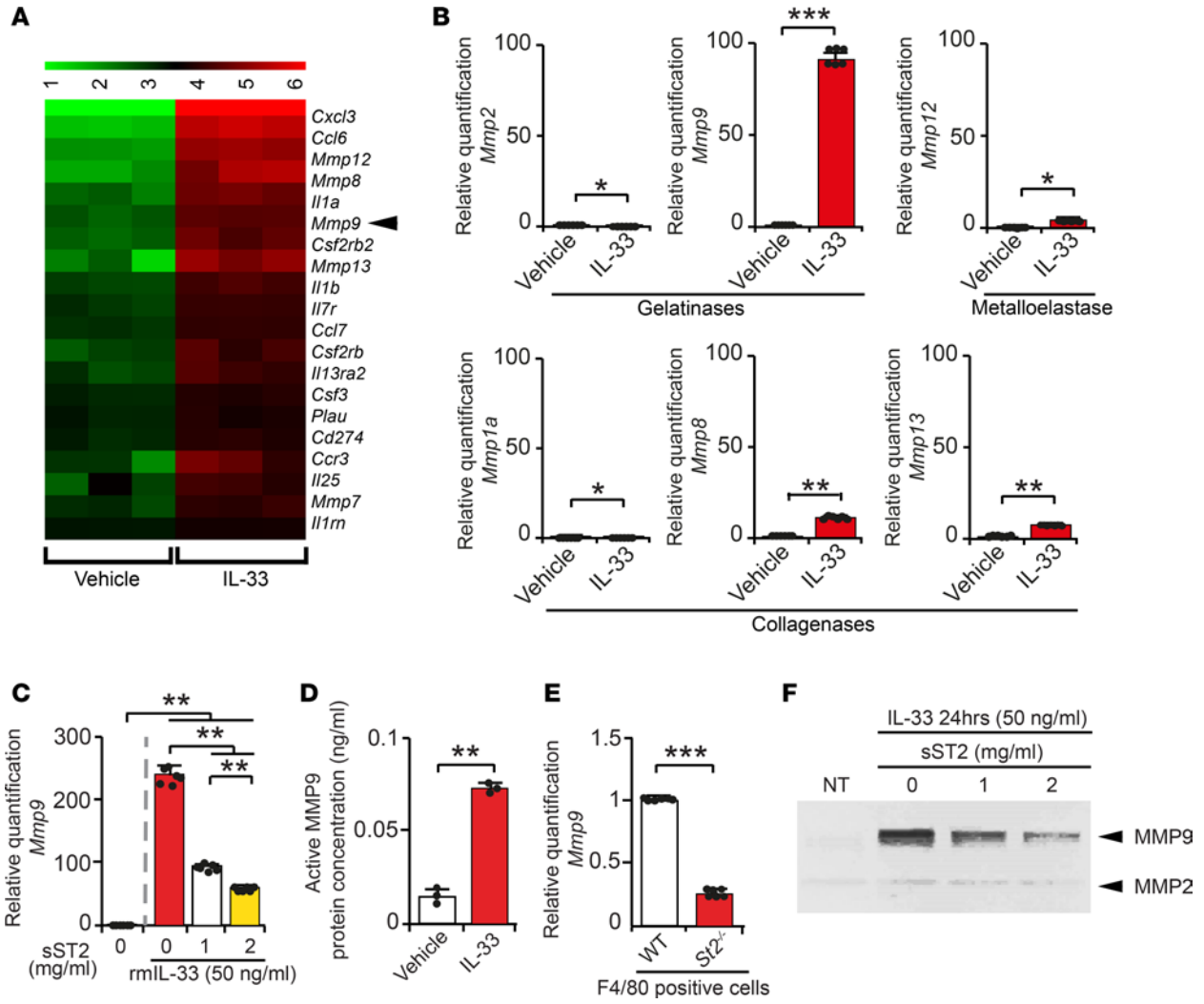

Figure 2. IL-33 upregulates MMP9 in macrophages through ST2 activation. (**A**) Heatmap of a subset of cancer metastasis–related genes by genome-wide expression profiling of IL-33–stimulated macrophages (n = 3 samples per group). (**B**) qPCR quantification of mRNA expression levels of *Mmps* in IL-33–stimulated macrophages (n = 6 samples per group). (**C**) Inhibition of *Mmp9* mRNA expression of IL-33–stimulated macrophages by a soluble ST2 (IL-33 trap) (n = 6 samples per group). sST2, soluble ST2. (**D**) ELISA quantification of active MMP9 protein in the conditional medium from IL-33–stimulated macrophages (n = 3 samples per group). (**E**) qPCR quantification of *Mmp9* mRNA levels in F4/80$^+$ cells isolated from Panc02 tumors grown in WT or *St2*$^{-/-}$ mice (n = 6 samples per group). (**F**) Detection of MMP9 protease activity by a gelatin-based zymography assay in conditional medium derived from IL-33–stimulated macrophages in the presence or absence of a soluble ST2 (n = 3 samples per group). NT, nontreated. Mean ± SEM. *P < 0.05; **P < 0.01; ***P < 0.001, Student's t test.

A completely inhibited *Mmp9* production to the control level. Our data demonstrate that NF-κB is the transcription factor for the *Mmp9* gene. Altogether, these findings define the signaling pathway of the IL-33-ST2-NF-κB-MMP9 axis in macrophages (Figure 3K). In support of our findings, a recent study shows that IL-33 induces MMP9 expression through activation of AP-1–mediated transcription (21).

IL-33-ST2–dependent recruitment of TAMs and MMP9 production in tumors. Having defined molecular mechanisms and signaling pathways of IL-33–induced MMP9 production, we performed a series of in vivo tumor studies to investigate the cellular source of MMP9 in TME. In the Panc02 PDAC model, genetic deletion of *Il33* or *St2* genes resulted in a significant reduction of the total number of total TAMs (Figure 4A). Notably, the total reduction of M2 macrophages appeared to be greater than the total reduction in TAMs in the ST2 KO model (>65% vs. <50%). In addition to genetic loss-of-function approaches, Panc02 tumor-bearing mice were treated with a sST2 receptor. Similarly, IL-33 trap treatment also effectively blocked TAM recruitment and M2 polarization (Figure 4B). An independent pharmacological approach using clodronate liposome also effectively eliminated total macrophage population (Supplemental Figure 4). These results show that endogenous IL-33 significantly contributes to TAM recruitment and M2 polarization.

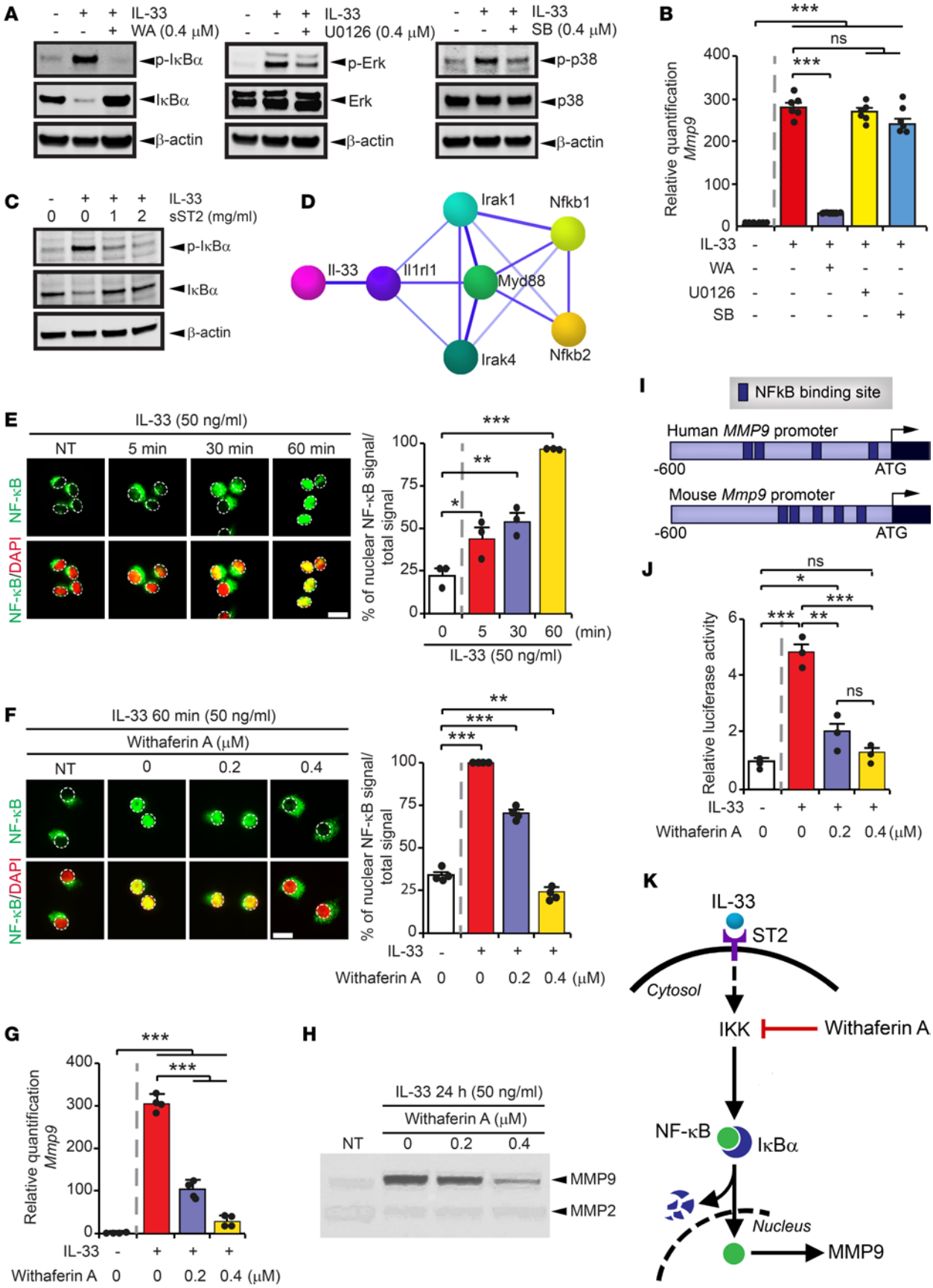
A
IL-33
WA (0.4 μM)
U0126 (0.4 μM)
SB (0.4 μM)
p-IκBα
IκBα
β-actin
p-Erk
Erk
p-p38
p38
B
Relative quantification Mmp9
ns
***
IL-33
WA
U0126
SB
C
sST2 (mg/ml)
D
Irak1
Nfkb1
Il-33
Il1rl1
Myd88
Irak4
Nfkb2
E
IL-33 (50 ng/ml)
NT
5 min
30 min
60 min
NF-κB
NF-κB/DAPI
% of nuclear NF-κB signal/ total signal
(min)
F
IL-33 60 min (50 ng/ml)
Withaferin A (μM)
G
H
IL-33 24 h (50 ng/ml)
MMP9
MMP2
I
NFkB binding site
Human MMP9 promoter
Mouse Mmp9 promoter
-600
ATG
J
Relative luciferase activity
K
IL-33
ST2
Cytosol
IKK
Withaferin A
NF-κB
IκBα
Nucleus
MMP9

Figure 3. Transcriptional regulation of the *Mmp9* promoter activity by IL-33- NF-κB signaling. (**A**) Western immunoblot analysis of phosphorylation of IκBα, Erk, and p38 in vehicle- and IL-33–treated macrophages in the presence or absence of their specific inhibitors. β-Actin served as a loading control (n = 3 samples per group). WA, withaferin A; SB, SB203580. (**B**) qPCR quantification of *Mmp9* mRNA levels of IL-33–stimulated macrophages in the presence or absence of their specific inhibitors (n = 6 samples per group). (**C**) Western immunoblot analysis of phosphorylation of IκBα in IL-33–stimulated macrophages in the presence or absence of a soluble ST2 (sST2). β-Actin served as a loading control (n = 3 samples per group). (**D**) A network scheme demonstrating protein-protein interactions linking IL-33 to NF-κB. Irak, IL-1 receptor–associated kinase; MyD88, myeloid differentiation primary response 88. (**E**) Immunostaining of NF-κB (green) in IL-33–stimulated macrophages at 5-, 30-, or 60-minute time points. Cell nuclei were counterstained with DAPI (red; scale bar: 25 μm). Overlapping yellow signals were randomly quantified (n = 3 fields per group). (**F**) Immunostaining of NF-κB (green) in IL-33–stimulated macrophages in the presence or absence of different concentrations of withaferin A. Cell nuclei were counterstained with DAPI (red; scale bar: 50 μm). Overlapping yellow signals were quantified (n = 4 random fields per group). (**G**) Detection of MMP9 protease activity by a gelatin-based zymography assay in conditional medium derived from IL-33–stimulated macrophages in the presence or absence of different concentrations of withaferin A (n = 4 samples per group). (**H**) qPCR quantification of *Mmp9* mRNA levels in IL-33–stimulated macrophages in the presence or absence of different concentrations of withaferin A (n = 6 samples per group). (**I**) Schematic indicating 5 NF-κB–binding sites located in the proximal region of the mouse *Mmp9* promoter. (**J**) *Mmp9* promoter activity in macrophages by the luciferase reporter assay. Relative luciferase activity was measured after IL-33 stimulation in the presence or absence of different concentrations of withaferin A (n = 3 samples per group). (**K**) Schematic showing the IL-33-ST2-NF-κB-MMP9 signaling pathway. IKK, IκB kinase. Mean ± SEM. *P < 0.05; **P < 0.01; ***P < 0.001, Student's t test.

Along with reduction of TAMs, *Mmp9* expression was markedly impaired in the tumor tissues (Figure 4C), suggesting IL-33–recruited TAMs were responsible for MMP9 production. An independent mouse fibrosarcoma model overexpressing IL-33 also led to high expression of MMP9 (Supplemental Figure 5), validating IL-33 as the primary trigger for MMP9 production. This notion was supported by clodronate-treated tumors, which also were showing a substantial decrease of *Mmp9* expression (Figure 4D). To causally link TAMs and NF-κB in regulation of MMP9 production in vivo, DHMEQ, an NF-κB–specific inhibitor, was employed for treatment of tumor-bearing mice. Again, DHMEQ treatment effectively blocked *Mmp9* synthesis in tumors (Figure 4E). Final evidence of the TAM-MMP9 axis came from examining MMP9 enzymatic activity. Deletion of TAMs completely ablated MMP9 enzymatic activity by two independent activity assays (Figure 4, F and G).

The IL-33-ST2-NF-κB-MMP9 pathway in cancer metastasis. We next investigated the functional effect of IL-33-ST2-NF-κB-MMP9 in cancer invasion and metastasis using the Panc02 PDAC model. Subcutaneous implantation of Panc02 in syngeneic mice resulted in extensive pulmonary metastasis. Gross examination of lung tissues showed that 50% of tumor-bearing mice had visible surface metastatic nodules (Figure 5A). In contrast, the same Panc02 PDAC tumors grown in IL-33 KO mice did not cause extensive pulmonary metastases (Figure 5A), suggesting that IL-33 was responsible for lung metastasis. ST2 KO mice produced similar inhibitory effects on cancer metastasis (Figure 5A). To further strengthen our findings, we treated Panc02 tumor-bearing mice with the IL-33 trap and examined lung tissues. Similar to the *Il33*$^{-/-}$ genetic model, IL-33 trap treatment effectively blocked lung metastasis (>40% reduction of lung surface metastases) (Figure 5B). As macrophages were the primary target of IL-33 in TME, we depleted TAMs by pharmacological treatment of mice with clodronate liposome. Again, clodronate effectively ablated pulmonary metastatic nodules (Figure 5C). These findings demonstrated the crucial role of IL-33-ST2–recruited TAMs in cancer metastasis.

To define the downstream effectors mediating cancer metastasis, we performed both genetic and pharmacological loss-of-function experiments. Pharmacological treatment of mice with DHMEQ-NF-κB and SB-3CT-MMP9 inhibitors (22, 23) resulted in marked inhibition of lung metastasis (Figure 5, D and E). Consistently, genetic deletion of *Mmp9* in mice but not in tumor cells also markedly inhibited lung metastasis (Figure 5F). These data provide compelling evidence of IL-33-ST2-NF-κB-MMP9 axis–mediated cancer metastasis, and targeting each of the signaling components of this pathway would be effective for treatment of metastasis.

Degradation of the vascular BM by MMP9. Knowing the presence of exceptionally high levels of activated MMP9 and detailed molecular pathways of the IL-33-ST2-NF-κB-MMP9 axis, the functional impact of MMP9 on vascular BM was investigated. Immunohistochemical staining of Panc02 tumor tissues with specific antibodies detecting each of the BM components showed that tumor vessels completely lacked the laminin component, whereas collagen IV and fibronectin were abundantly expressed in tumor vessels (Figure 6 and Supplemental Figure 6, A and B). To study the causational link between the loss of laminin and the activation of IL-33-ST2-NF-κB-MMP9 pathway, pharmacological and genetic loss-of-function approaches were employed to remove or block each of the signaling components. Genetic deletion of the *Il33* gene (15) in mice completely recovered the laminin expression in tumor vessels. These findings indicate that IL-33 not only is the crucial cytokine responsible for the loss of laminin, but also demonstrate

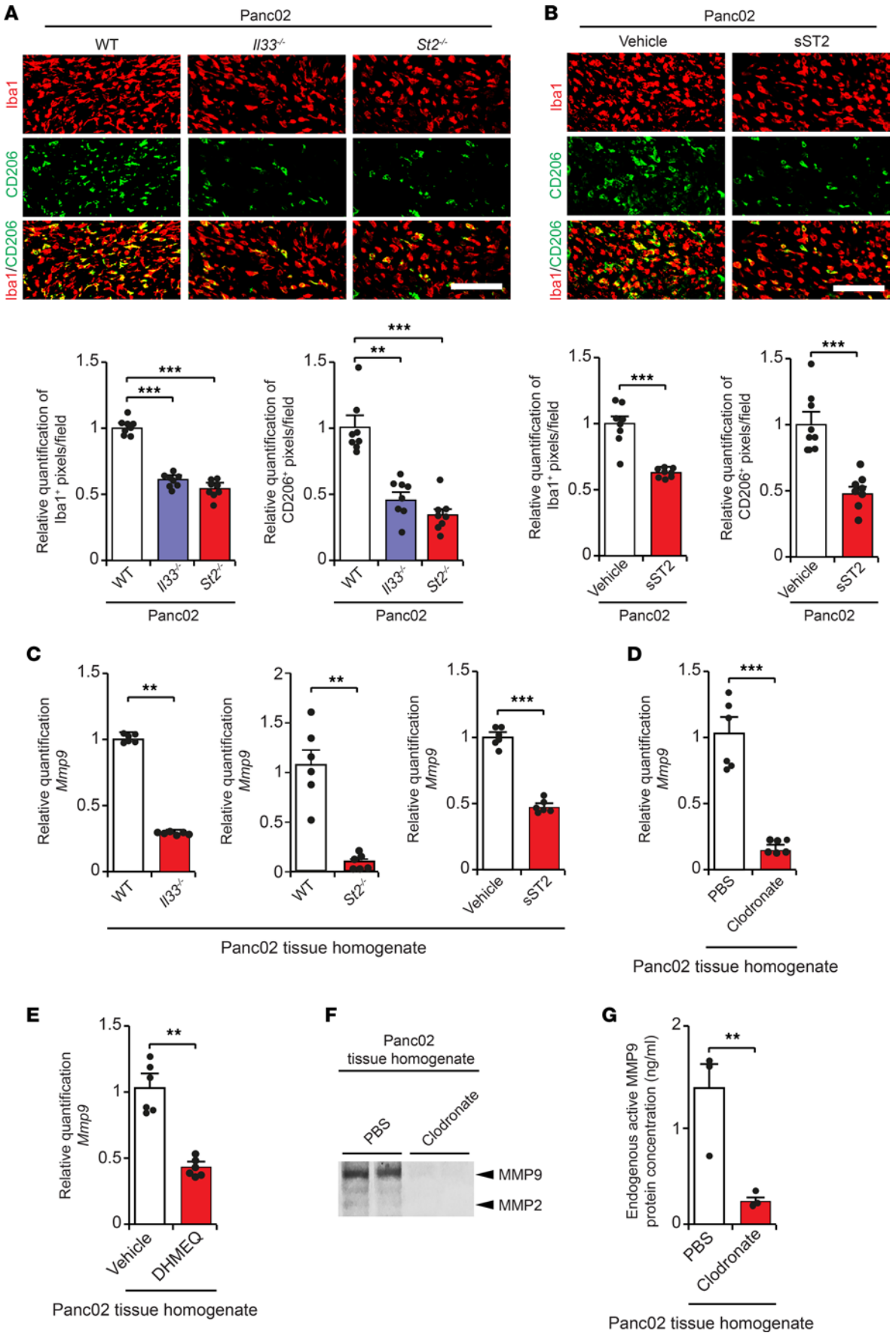
A
Panc02
WT
Il33-/-
St2-/-
Iba1
CD206
Iba1/CD206
B
Panc02
Vehicle
sST2
Relative quantification of Iba1+ pixels/field
Relative quantification of CD206+ pixels/field
C
Relative quantification Mmp9
Panc02 tissue homogenate
D
PBS
Clodronate
E
DHMEQ
F
Panc02 tissue homogenate
MMP9
MMP2
G
Endogenous active MMP9 protein concentration (ng/ml)

Figure 4. IL-33-ST2–dependent production of MMP9 in macrophages. (**A**) Immunohistochemical staining and quantification of Iba1$^+$ (red) and CD206$^+$ (green) macrophages in Panc02 tumors grown in WT, *Il33*$^{-/-}$, or *St2*$^{-/-}$ mice (n = 8 random fields per group; scale bar: 100 μm). (**B**) Immunohistochemical staining and quantification of Iba1$^+$ (red) and CD206$^+$ (green) macrophages in vehicle- and soluble ST2–treated (sST2-treated) Panc02 tumors (n = 8 random fields per group; scale bar: 100 μm). (**C**) qPCR quantification of *Mmp9* mRNA levels in Panc02 tumors grown in WT, *Il33*$^{-/-}$, or *St2*$^{-/-}$ mice or WT mice treated with a soluble ST2 (n = 6 samples per group). (**D**) qPCR quantification of *Mmp9* mRNA levels of PBS- and clodronate-treated Panc02 tumors (n = 6 samples per group). (**E**) qPCR quantification of *Mmp9* mRNA levels in Panc02 tumors treated with vehicle and DHMEQ (a NF-κB inhibitor) (n = 6 samples per group). (**F**) Detection of MMP9 protease activity by a gelatin-based zymography assay in PBS- and clodronate-treated Panc02 tumors (n = 4 samples per group). (**G**) ELISA quantification of active MMP9 protein in PBS- and clodronate-treated Panc02 tumors (n = 3 samples per group). Mean ± SEM. $^{**}P < 0.01$; $^{***}P < 0.001$, Student's t test.

that a nontumor cell–derived factor controls the BM integrity (Figure 6A). Similar rescue results were also obtained in ST2 KO mice. Likewise, pharmacological treatment of PDAC with the IL-33 trap reproduced nearly identical results of laminin recovery in tumor vessels (Figure 6B). These data demonstrate the essential role of IL-33-ST2 signaling in diminishing the laminin component in BM.

To further investigate the relation between TAMs and laminin loss, tumor-bearing mice were treated with clodronate to remove macrophages (14). Strikingly, clodronate treatment led to recovery of laminin expression in tumor vessels (Figure 6C), indicating that macrophages were responsible for degradation of laminin. Along with the IL-33-ST2-NF-κB-MMP9 signaling pathway, NF-κB was also pharmacologically inhibited. Again, inhibition of NF-κB resulted in laminin recovery in tumor vessels (Figure 6D). As vascular laminin has previously been described as a target of MMP9 (24), pharmacological and genetic approaches were applied to investigate the link between MMP9 and laminin in our models. Tumors receiving treatment with an MMP9 inhibitor and those grown in mice with genetic deletion of *Mmp9* displayed a significant recovery of their laminin expression in tumor vessels (Figure 6, E and F). Together, these results show that the IL-33-ST2-NF-κB-MMP9 axis is responsible for degradation of BM in tumor vessels.

The IL-33-MMP9 axis in human cancer metastasis. Having investigated the functional effect of IL-33-ST2-NF-κB-MMP9 signaling on cancer metastasis in mouse tumor models, we validated these findings in human cancer models to recapitulate the clinical relevance. First, we analyzed IL-33 production in various human tumor tissues grown in immunodeficient mice. It appeared that human tumors grown in SCID mice had large differences in their IL-33 protein expression levels (Figure 7A and Supplemental Figure 7). Interestingly, human MiaPaCa2, PaCa3, and Panc1 PDAC tumor tissues produced high levels of mouse IL-33. Additionally, some other cancers, including squamous carcinoma, lung cancer, breast cancer, and colorectal cancer, also produced substantial amounts of IL-33 proteins (Supplemental Figure 7). In contrast, 4 independent fibroblast-less melanomas produced insignificant amounts of IL-33 (Supplemental Figure 7). IL-33–high MiaPaCa2 showed overwhelming amounts of fibrotic components in tumor tissues, whereas IL-33–low UACC257 melanoma lacked a detectable fibrosis in tumor tissues (Figure 7B). These findings again linked the IL-33 production to the content of tumor fibrosis. There was a correlation between IL-33 expression levels and MMP9 production in PDAC tumors (Figure 7C).

Similar to the mouse Panc02 PDAC model, treatment of human MiaPaCa2 PDAC with the IL-33 trap significantly ablated the total number of macrophages (Figure 7D). In contrast to the decrease of macrophage numbers, BM-laminin was markedly increased around tumor vessels in the IL-33 trap-treated tumors (Figure 7E). Treatment of human MiaPaCa2 tumors with MMP9 inhibitor also resulted in recovery of the laminin component in BM around tumor vessels (Figure 7F). Treatments with IL-33 trap and SB-3CT markedly reduced the metastasis of human PDAC (Figure 7, G and H). Together, these findings demonstrate the pathophysiological relevance of the IL-33-MMP9 axis to cancer metastasis.

Discussion

Our present work provides an example of how tumor cells manipulate CAFs, TAMs, and blood vessels in an intimately coordinated manner through defined molecular mechanisms for metastasis. While it is known that M2 TAMs promote metastasis, TAM recruitment and M2 phenotypic activation remain largely unexplored. We recently showed that tumor stromal PDGFRβ$^+$ fibroblasts and perivascular cells are the main cellular sources for production of IL-33, a cytokine targeting monocytes/macrophages through the ST2 receptor (14). These findings suggest the PDGFRβ$^+$ stromal fibroblasts and pericytes in TME significantly modulate tumor inflammation. Among different cancer types, PDAC possesses an exceptionally high content of fibrotic cellular components that produce high levels of IL-33. Using experimental mouse and human PDAC models, we have validated the fact of the fibrotic origin of IL-33. This conclusion may be extended to other fibrous tumors.

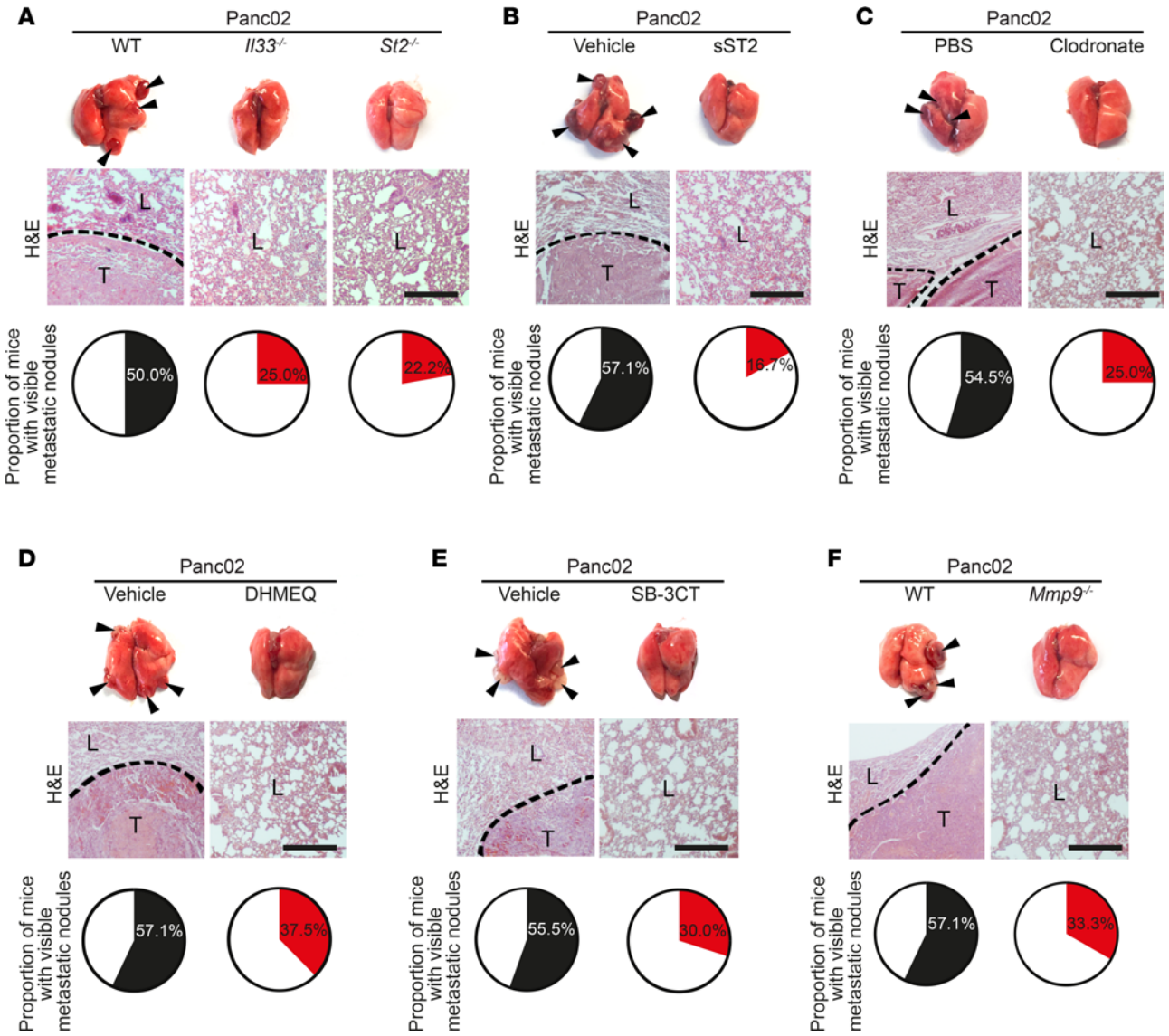

Figure 5. Activation of IL-33-ST2-NF-κB-MMP9 signaling promotes metastasis. (**A**) Visible surface pulmonary metastatic nodules and lung histology of Panc02 tumor-bearing WT, *Il33*$^{-/-}$, or *St2*$^{-/-}$ mice. Arrowheads indicate lung surface metastatic nodules. Dashed line marks the border between the metastatic nodule (T) and surrounding lung tissues (L) (scale bar: 250 μm). Quantification of the percentage of animals with visible pulmonary metastasis (n = 6–10 mice per group). (**B**) Visible surface pulmonary metastatic nodules and lung histology of Panc02 tumor-bearing mice receiving vehicle or soluble ST2 (sST2) treatments. Arrowheads indicate lung surface metastatic nodules. Dashed line marks the border between the metastatic nodule and surrounding lung tissues (scale bar: 250 μm). Quantification of the percentage of animals with visible pulmonary metastasis (n = 6–10 mice per group). (**C**) Visible surface pulmonary metastatic nodules and lung histology of Panc02 tumor-bearing mice receiving PBS or clodronate treatments. Arrowheads indicate lung surface metastatic nodules. Dashed line marks the border between the metastatic nodule and surrounding lung tissues (scale bar: 250 μm). Quantification of the percentage of animals with visible pulmonary metastasis (n = 6–10 mice per group). (**D**) Visible surface pulmonary metastatic nodules and lung histology of Panc02 tumor-bearing mice receiving vehicle or DHMEQ (a NF-κB inhibitor) treatments. Arrowheads indicate lung surface metastatic nodules. Dashed line marks the border between the metastatic nodule and surrounding lung tissues (scale bar: 250 μm). Quantification of the percentage of animals with visible pulmonary metastasis (n = 6–10 mice per group). (**E**) Visible surface pulmonary metastatic nodules and lung histology of Panc02 tumor-bearing mice receiving vehicle or SB-3CT (a MMP9 inhibitor) treatments. Arrowheads indicate lung surface metastatic nodules. Dashed line marks the border between the metastatic nodule and surrounding lung tissues (scale bar: 250 μm). Quantification of the percentage of animals with visible pulmonary metastasis (n = 6–10 mice per group). (**F**) Visible surface pulmonary metastatic nodules and lung histology of Panc02 tumor-bearing WT or *Mmp9*$^{-/-}$ mice. Arrowheads indicate lung surface metastatic nodules. Dashed line marks the border between the metastatic nodule and surrounding lung tissues (scale bar: 250 μm). Quantification of percentage of animals with visible pulmonary metastasis (n = 6–10 mice per group).

Although CAFs are known to commit an invasive phenotype and metastasis, molecular mechanisms underlying CAF-mediated metastasis are largely undisclosed. More interestingly, fibrosis and inflammation are two intertwined processes that often synchronize in TME (1, 25–27). However, it is unclear which of these two processes serves as the initiative trigger to evoke the other process.

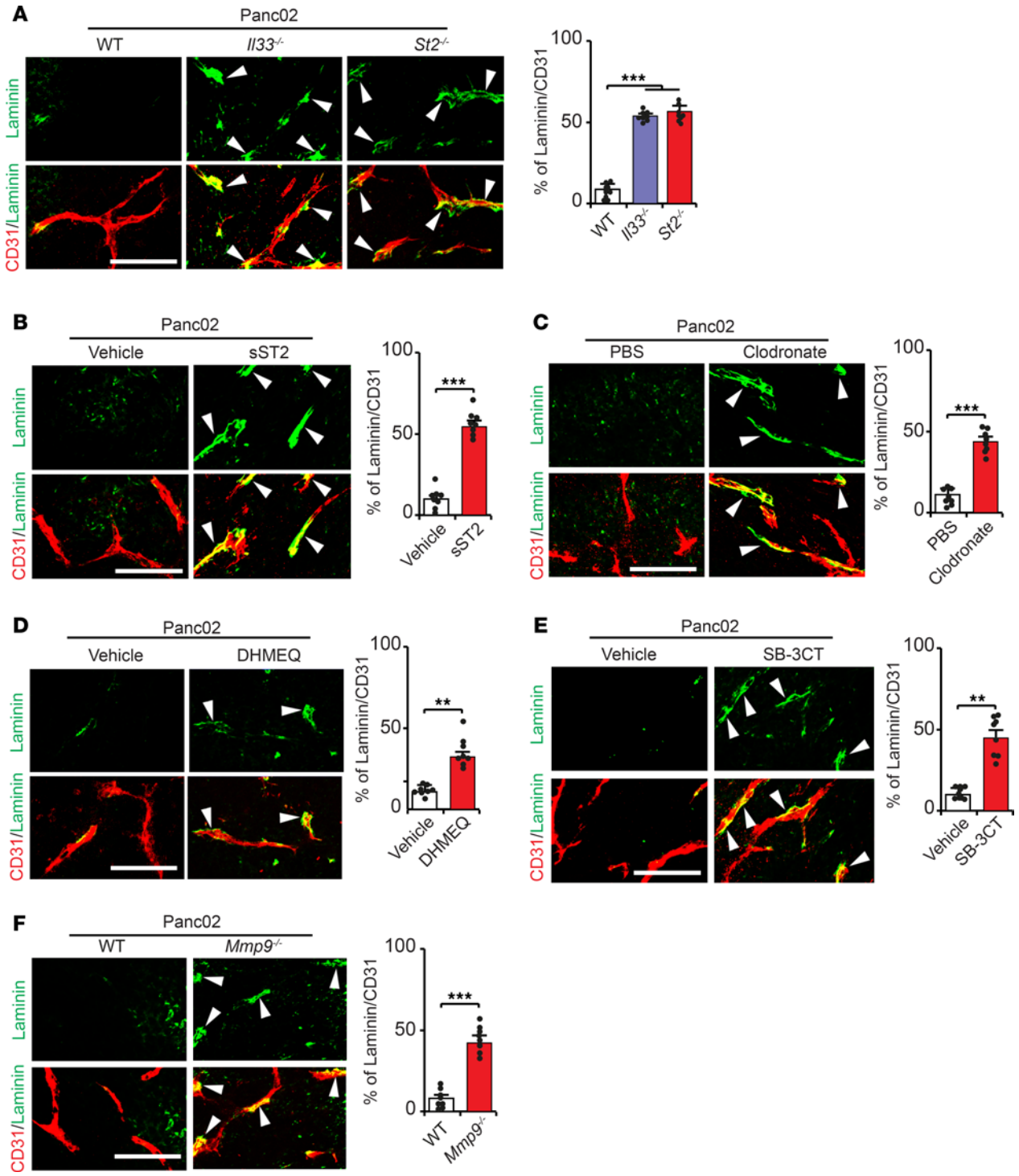

Figure 6. Degradation of the basement membrane by the IL-33-ST2-NF-κB-MMP9 axis. (**A**) Immunohistochemical staining and quantification of CD31⁺ (red) and laminin⁺ (green) structures in Panc02 tumors grown in WT, *Il33*$^{-/-}$, or *St2*$^{-/-}$ mice. Arrowheads indicate laminin/CD31 double-positive signals. Quantification of the percentage of laminin⁺/CD31⁺ signals per field (n = 8 random fields per group; scale bar: 100 μm). (**B**) Immunohistochemical staining and quantification of CD31⁺ (red) and laminin⁺ (green) structures in vehicle- or soluble ST2–treated Panc02 tumors Arrowheads indicate laminin/CD31 double-positive signals. Quantification of the percentage of laminin⁺/CD31⁺ signals per field (n = 8 random fields per group; scale bar: 100 μm). (**C**) Immunohistochemical staining and quantification of CD31⁺ (red) and laminin⁺ (green) structures in PBS- or clodronate-treated Panc02 tumors. Arrowheads indicate laminin/CD31 double-positive signals. Quantification of the percentage of laminin⁺/CD31⁺ signals per field (n = 8 random fields per group; scale bar: 100 μm). (**D**) Immunohistochemical staining and quantification of CD31⁺ (red) and laminin⁺ (green) structures in Panc02 tumors treated with vehicle or DHMEQ (a NF-κB inhibitor). Arrowheads indicate laminin/CD31 double-positive signals. Quantification of the percentage of laminin⁺/CD31⁺ signals per field (n = 8 random fields per group; scale bar: 100 μm). (**E**) Immunohistochemical staining and quantification of CD31⁺ (red) and laminin⁺ (green) structures in Panc02 tumors treated with vehicle or SB-3CT (a MMP9 inhibitor). Arrowheads indicate laminin/CD31 double-positive signals. Quantification of the percentage of laminin⁺/CD31⁺ signals per field (n = 8 random fields per group; scale bar: 100 μm).

(**F**) Immunohistochemical staining and quantification of CD31$^+$ (red) and laminin$^+$ (green) structures in Panc02 tumors grown in WT or *Mmp9*$^{-/-}$ mice. Arrowheads indicate laminin/CD31 double-positive signals. Quantification of the percentage of laminin$^+$/CD31$^+$ signals per field (n = 8 random fields per group; scale bar: 100 μm). Mean ± SEM. $^{**}P < 0.01$; $^{***}P < 0.001$, Student's t test.

In this study, we provide compelling evidence showing that CAF-derived IL-33 markedly augments TAM recruitment and M2 phenotypic activation. Ablation of TAM recruitment and M2 transition by genetic deletion of *Il33* in nonmalignant cells supports the notion of stromal cell interaction in TAM recruitment. Paracrine loops among CAFs, TAMs, and tumor cells modulate their interactions (Figure 8). For example, tumor cell–derived PDGFs activate PDGFRβ$^+$ CAFs and pericytes to upregulate IL-33 expression though a SOX-7–dependent transcriptional mechanism (14). Once activated, macrophages may produce FGFs and TGF-β to amplify the CAF compartment, creating mutually positive feedback systems. Additionally, vascular cells significantly contribute to both fibrosis and inflammation in TME (28, 29). Our recent work shows that PDGF-stimulated perivascular cells produce IL-33, which is produced at levels higher than those of other upregulated gene products (14). Thus, perivascular cells communicate with inflammatory cells to facilitate tumor inflammation. Intriguingly, pericytes in TME can also transdifferentiate into fibroblasts though the mechanism of pericyte-fibroblast transition (PFT) (28). Particularly, PFT-derived CAFs exhibit myofibroblast features that facilitate cancer metastasis. Thus, tumor vessels coordinate the amplification of both CAF and TAM pools, which would inevitably alter tumor growth and metastasis.

One of the central issues in understanding M2 TAM–mediated cancer metastasis is clarifying the interaction between M2 macrophages and tumor vessels. How do macrophages disintegrate the BM sheet and eventually allow tumor cells to intravasate? At this time of writing, this critical issue remains unresolved, although other independent studies show stream migration of macrophages and tumor cells toward tumor vessels for intravasation (30, 31). Another paracrine mechanism that operates through EGFR and CSFR1 signaling pathways addresses the interaction between macrophages and tumor cells (32, 33). At the molecular level, the identity of molecular players needs to be uncovered. A more than 200-fold increase of *Mmp9* expression in IL-33–stimulated macrophages is one of the highlights of our results. Elevation and activation of MMP9 to an extremely high level suggests that this protease plays a crucial role in TME. Mechanistically, we have defined a signaling pathway in which IL-33 activated ST2 and downstream NF-κB is essentially required for transcriptional upregulation of MMP9 (Figure 8). Although this mechanism of upregulation is specific for MMP9, we cannot exclude the existence of alternative mechanisms, particularly signaling pathways involving upregulation of other MMPs. It is likely that the proteolytic activity of MMP9 in TME is underestimated because simultaneous downregulation of TIMPs by IL-33 could further augment its enzymatic activity. Once activated, MMP9 degrades the extracellular matrix protein laminin, which is a major BM component of blood vessels. A series of loss-of-function experiments by genetic deletion of IL-33, ST2, and MMP9 completely rescue laminin expression in tumor vessels. Within TAMs, IL-33-ST2–augmented NF-κB, at transcriptional levels, controls MMP9 expression. These findings establish a signaling pathway of IL-33-ST2-NF-κB-MMP9–mediated BM degradation. Disintegration of tumor vessel BM permits intravasation of tumor cells into the circulation. Considering the early onset of metastasis in PDAC patients, dissemination of cancer cells in primary tumors may occur at a very early stage of tumor development, owing to infiltration of inflammatory cells and lack of BM. If so, inhibition of any signaling component within the IL-33-ST2-NF-κB-MMP9 signaling pathway would provide a novel therapeutic option for effective treatment of PDAC. This therapeutic concept may also apply to other solid tumors.

An extended discussion of our findings linking to cancer metastasis may also apply to the cancer extravasation. Metastatic cancer cells often remain associated with fibroblasts/myofibroblasts in the circulation and distal metastatic sites (11, 34). If these disseminated CAFs continue to maintain original features at the extravasation site, IL-33 may trigger a local inflammation at the luminal inner layer of the vessel wall. Consequently, IL-33–augmented MMP9 may also disintegrate the vessel wall from the luminal site. Thus, it is highly plausible that CAFs contribute to cancer cell extravasation. Another possibility is that disseminated circulating tumor cells remain associated with TAMs (10) that directly manipulate disintegration of vessel wall for extravasation. These interesting possibilities warrant future investigation. At the time of this writing, it is unclear if the interaction between CAFs and TAMs would play a role in preparation of premetastatic niches, as shown in other tumor models (35, 36).

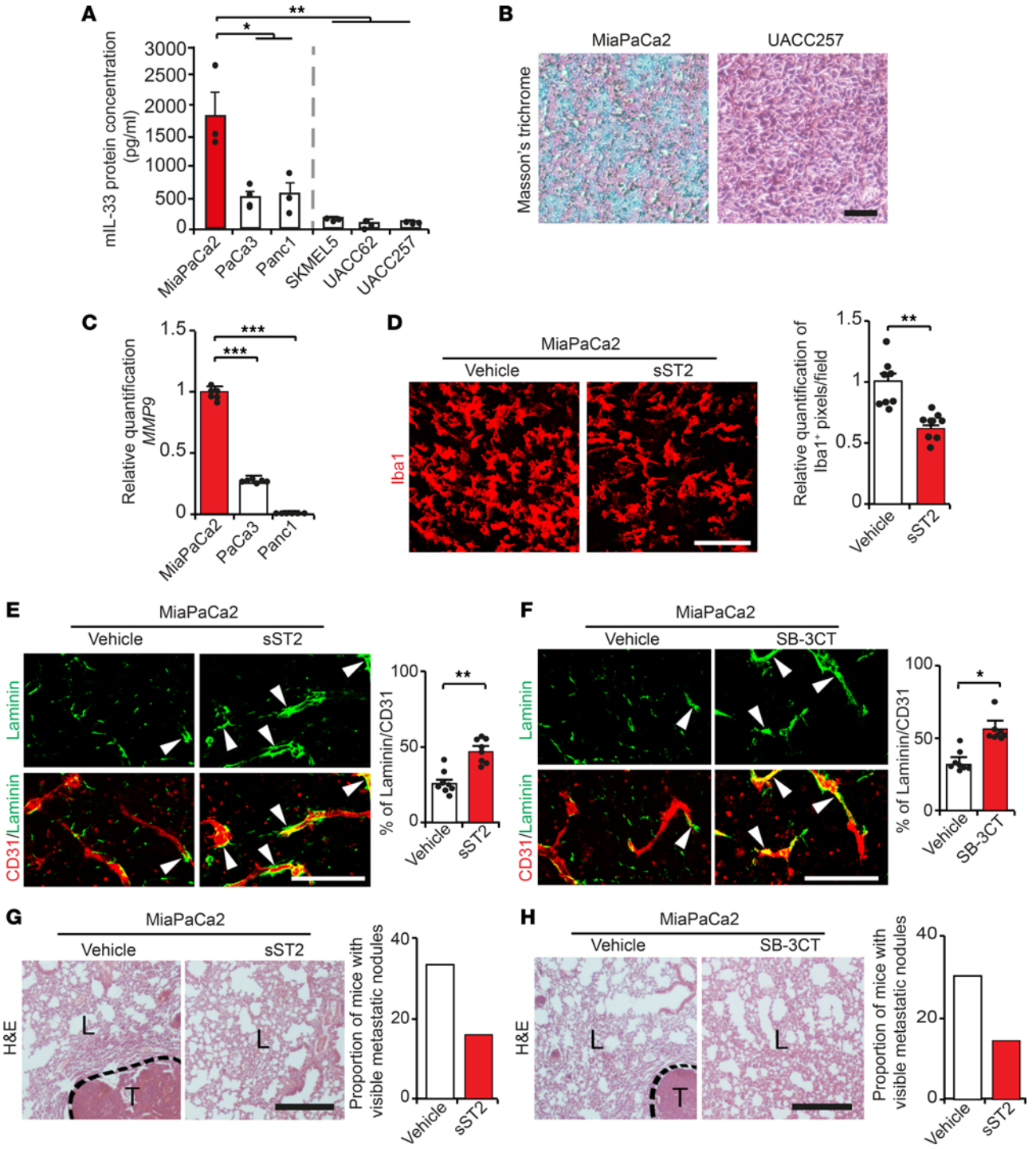

Figure 7. IL-33–induced MMP9 in macrophages promotes metastasis in human PDAC. (**A**) IL-33 protein levels in human melanoma and pancreatic cancers (n = 3 samples per group). (**B**) Staining of MiaPaCa2 PDAC and UACC257 melanoma tumor tissues. Light blue indicates fibrotic components (Masson's trichrome; scale bar: 50 μm). (**C**) qPCR quantification of *Mmp9* mRNA expression in 3 human pancreatic tumors (n = 6 samples per group). (**D**) Immunohistochemical staining and quantification of Iba1$^+$ (red) macrophages in vehicle- and a soluble ST2–treated MiaPaCa2 tumors (n = 8 random fields per group; scale bar: 100 μm). (**E**) Immunohistochemical staining and quantification of CD31$^+$ (red) and laminin$^+$ (green) structures in vehicle- and a soluble ST2–treated MiaPaCa2 tumors. Arrowheads indicate laminin/CD31 double-positive signals. Quantification of the percentage of laminin$^+$/CD31$^+$ signals per field (n = 8 random fields per group; scale bar: 100 μm). (**F**) Immunohistochemical staining and quantification of CD31$^+$ (red) and laminin$^+$ (green) structures in vehicle- and SB-3CT–treated MiaPaCa2 tumors. Arrowheads indicate laminin/CD31 double-positive signals. Quantification of the percentage of laminin$^+$/CD31$^+$ signals per field (n = 8 random fields per group; scale bar: 100 μm). (**G**) Lung histology of MiaPaCa2 tumor-bearing mice receiving vehicle or a soluble ST2 treatments. Dashed line marks the border between the metastatic nodule (T) and surrounding lung tissues (L) (scale bar: 250 μm). Quantification of percentage of animals with visible pulmonary metastasis (n = 6–10 mice per group). (**H**) Lung histology of MiaPaCa2 tumor-bearing mice receiving vehicle or SB-3CT treatments. Dashed line marks the border between the metastatic nodule and surrounding lung tissues (scale bar: 250 μm). Quantification of the percentage of animals with visible pulmonary metastasis (n = 6–10 mice per group). Mean ± SEM. $^*P < 0.05$; $^{**}P < 0.01$; $^{***}P < 0.001$, Student's t test.

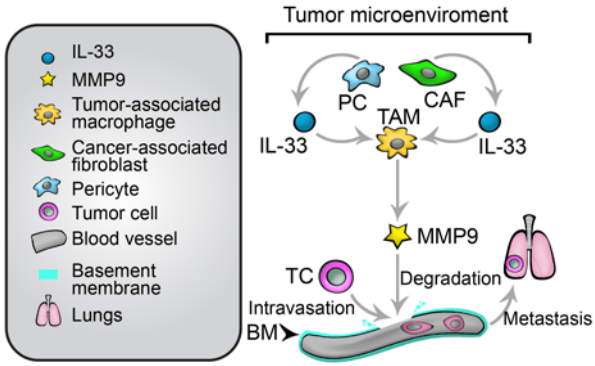

Figure 8. Mechanisms of IL-33–mediated crosstalk between CAFs and TAMs in cancer metastasis. Mechanistic insights on IL-33–mediated crosstalk between pericytes (PCs)/cancer-associated fibroblasts (CAFs) and tumor-associated macrophages (TAMs) in cancer metastasis. PDGFRβ$^+$ PCs/CAFs produce high levels of IL-33, which recruits TAMs and induces M2 macrophage polarization through its ST2 receptor. IL-33–stimulated TAMs produce high levels of MMP9 through activation of NF-κB, which transcriptionally activates the MMP9 promoter. MMP9 in turn degrades laminin, one of the key components in the basement membrane (BM). Deterioration of BM around the tumor vasculature allows tumor cells (TCs) to intravasate into the circulation. Circulating tumor cells (CTCs) eventually recolonize in distal organs, such as lungs, for further growth to become the clinically detectable metastatic mass.

Infiltration of fibrotic cells in tumors is inversely correlated with prognosis of cancer patients. In theory, it is difficult to understand the relationship of the sparse malignant cells and worsening prognosis. It would have been more reasonable if an opposite correlation existed, i.e., positive correlation of the high tumor cell component and poor prognosis. In PDAC, metastasis occurs in almost all cases at the very early stage of primary tumors that contain a high proportion of the fibrotic component. Concomitant infiltration of inflammatory cells also endures when primary PDAC tumors are tiny. Fibrosis and inflammation are two crucial pathological processes for promoting cancer metastasis at the early stage of cancer development. Experimental evidence using zebrafish models supports this view, showing that TAMs and CAFs stimulate cancer cell dissemination, intravasation, and, eventually, metastasis when a primary tumor mass consists of only a few hundred of cells (10, 11). As most cancer patients die of metastasis, understanding complex mechanisms underlying cancer metastasis provides valuable information for therapeutic intervention. Our findings define several targets and pave avenues for possible treatment of metastatic disease.

Methods

Cell culture. The murine Panc02 cancer cell line was provided by M. Schnurr from the Department of Internal Medicine, University of Munich, Munich, Germany; the murine MC38 cell line was provided by R. Hernández at the Gene Therapy Unit, Center for Applied Medical Research, University of Navarra, Pamplona, Spain; the murine E0771 cell line was obtained from F. Li at the Roswell Park Comprehensive Cancer Center, Buffalo, New York, USA; the human UACC257 and OV8 cell lines were provided by X. Li at the National Institutes of Health, Bethesda, Maryland, USA; the human TMK1 cell line was provided by E. Tahara at the Hiroshima University, Hiroshima, Japan; the human MiaPaCa-2 and Panc1 cell lines were provided by U. Stenius from the Department of Molecular Medicine, Karolinska Institutet; the human PaCa3 cell line was provided by G. Selivanova from the Department of Microbiology, Tumor and Cell Biology (MTC) of Karolinska Institutet; and the murine monocyte/macrophage Raw264.7 cell line was provided by M. Rottenberg from MTC, Karolinska Institutet. The following cell lines were purchased from ATCC: A431, A549, B16, CT26, HT29, IMR32, LLC, MDAMD231, SKMEL2, SKMEL5, T241, UACC62, and U87. A431, A549, B16, CT26, HT29, LLC, MC38, MDAMB231, PaCa3, Panc02, T241, and U87 cells were grown in a standard DMEM supplemented with 10% FBS. E0771, IMR32, OV8, SKMEL2, SKMEL5, TMK1, UACC62, and UACC257 cells were cultured in RPMI 1640 medium supplemented with 10% FBS. MiaPaCa-2 and Panc1 cells were grown in DMEM supplemented with 10% FBS and 1% sodium pyruvate (100 mM). Raw264.7 cells were grown in DMEM supplemented with 10% FBS and 1% HEPES (1 M).

Animals. WT C57BL/6 and immunodeficient CB17/Icr-Prkdcscid/IcrCrl (SCID) mice were obtained from the breeding unit of the animal facility at MTC, Karolinska Institutet. C57BL/6-*Il33*$^{-/-}$ mice were provided by Susumu Nakae at the Institute of Medical Science, University of Tokyo, Tokyo, Japan.

C57BL/6-*T1/St2*$^{-/-}$ mice were provided by Padraic Fallon at the Trinity College Dublin, Dublin, Ireland. C57BL/6-*Mmp9*$^{-/-}$ mice (B6.FVB(Cg)-*Mmp9*^{tm1Tvu}/J) were purchased from The Jackson Laboratory.

Tumor models. C57BL/6 or SCID mice, 4 to 8 weeks old, were used for tumor experiments. Age-matched female or male mice were used for each experiment. Tumor cells in PBS (approximately 1×10^6 cells/0.1 ml) were subcutaneously injected on the dorsal back of each mouse. Tumor sizes were measured every other day, and tumor volumes were calculated using a standard formula (volume = length × width^2 × 0.52). When volumes reached the size of 1.5–1.8 cm^3, mice were either sacrificed or primary tumors were removed. Tumor removal was surgically performed under anesthesia; mice were given a painkiller, temgesic, for at least 2 days; and mice were kept for an additional 4–6 weeks. After sacrifice, lungs were collected and examined for visible surface metastatic nodules. Lung tissues were subsequently paraffin embedded, stained with H&E, and examined under light microscopy. All animals were sacrificed using a lethal dose of CO_2.

Treatments. For in vivo tumor experiments, mice were treated as follows. Macrophages were depleted by tail intravenous injection of 100 μl clodronate liposomes (dichloromethylene bisphosphonate; Clodronate Liposomes) in each mouse. After 3 days, 1×10^6 tumor cells were subcutaneously implanted into each mouse that received subsequent clodronate treatment every 4 days until tumor removal. A sST2 (0.1 mg/mouse) was used to neutralize IL-33 in vivo. sST2 was subcutaneously injected 1 day prior to tumor implantation and daily injections were continued at the same dose until tumor removal. To inhibit MMP9 in vivo, tumor-bearing mice were treated daily with SB-3CT by intraperitoneal injection (50 mg/kg, formulated in DMSO, PEG-200, and H_2O) for the first week, followed by treatment every other day until tumor removal. For inhibition of NF-κB, the DHMEQ inhibitor was daily intraperitoneally injected at a dose of 8 mg/kg (provided by Kazuo Umezawa, Aichi Medical University, Aichi, Japan).

FACS. FACS analysis was performed as previously described (37). Briefly, raw 264.7 cells were stained on ice for 45 minutes with an Alexa Fluor 647 anti-mouse F4/80 antibody (123122, BioLegend), a PE anti-mouse CD206 antibody (141705, BioLegend), an FITC-conjugated anti-mouse CCR3 antibody (144509, BioLegend), and an anti-mouse PDL2 antibody (107202, BioLegend). Samples were analyzed using FACScan and the CellQuest software (BD).

Magnetic-activated cell sorting. Freshly dissected tumor tissues were cut into small pieces and digested at 37°C for 60 minutes with a mixture of collagenases I and II (0.15% of each). The single-cell suspension was prepared with a 0.40-μm filter and was stained for 45 minutes on ice with an Alexa Fluor 647 anti-mouse F4/80 antibody (123122, BioLegend) or an anti-mouse PDGFRβ antibody (14-1402-82, eBioscience) followed by an Alexa Fluor 647–conjugated goat anti-rat antibody (A21247, invitrogen). Anti-Alexa Fluor 647 MicroBeads (130-091-395, Miltenyi Biotec) were subsequently used for magnetic labeling. After washing, positive and negative cells were sorted with a magnetic-activated cell sorting (MACS) column and magnetic MACS separators (Miltenyi Biotec). Single-cell suspensions were collected for further detections.

ELISA. ELISA was used for measuring mIL-33 protein concentrations. Tissue samples and culture cells were homogenized in a lysis buffer (3228, MilliporeSigma), followed by 20-minute centrifugation. Supernatants were stored at –20°C or –80°C until further analysis. The mIL-33 ELISA (M3300, R&D Systems) was performed according to the manufacturer's protocol using the appropriate standard curve. Absorbance values were detected at 450 nm using a microplate reader.

Luciferase assay. A luciferase assay was performed using a pGL3-Luciferase plasmid containing the 0.6-kb promoter region of mouse *Mmp9* (a gift from Wolfgang Eberhardt, Goethe University, Frankfurt, Germany). The plasmid was packaged into a lentiviral vector using 293T cells. Macrophages were incubated overnight with the conditioned medium containing virus particles. Cells were allowed to recover for several hours prior to receiving treatment with a NF-κB inhibitor (Withaferin A, 2816, Tocris Bioscience), followed by stimulation with IL-33 for 18 hours. Luciferase activity was measured in a luminometer using a dual-luciferase reporter assay system according to the manufacturer's instructions (E1910, Promega).

MMP9 activity. A method similar to ELISA was used to measure endogenous MMP9 activity. For this purpose, total protein fractions were extracted from fresh tumor tissues or cells using a lysis buffer, and samples were kept on ice for immediate use or stored at –80°C. The mouse MMP9 activity assay (QZBmmp9M, QuickZyme Biosciences) was performed according to the manufacturer's protocol. In brief, samples and standards were added to individual wells of a 96-well microplate together with an assay buffer and incubated at 4°C overnight. Followed by rigorous washing with PBS, an assay buffer was added to sample-containing wells. An APMA solution (0.5 mM) was added to the standard-containing wells. A detection reagent was added to all wells. Absorbance at 405 nm was detected to record $t = 0$ hours, $t = 1$ hour, and $t = 6$ hours values, with interval incubation at 37°C.

Zymography. Total tissue homogenates or conditional media were collected to measure MMP9 activity using a zymography-based assay (Zymography, Invitrogen). An equal amount of protein from each sample was mixed with the LDS sample buffer (NP0007, Invitrogen), incubated at room temperature for at least 15 minutes, and subsequently loaded onto a Novex Zymogram gelatin gel (10%, EC6175, Invitrogen). Gels were incubated for 30 minutes at room temperature with a renaturing buffer (LC2670, Invitrogen), followed by washing and further incubating at 37°C overnight with a developing buffer (LC2671, Invitrogen). Gels were washed again and stained at room temperature for 3 hours with SimplyBlue SafeStain (LC6060, Invitrogen) or until bands were clearly visible.

Inhibiting intracellular signaling. To study intracellular signaling, cultured macrophages were starved overnight in 2% FBS-DMEM and pretreated with selective inhibitors against NF-κB (Withaferin A, 2816, Tocris Bioscience), MEK1/2 (U0126, 1144, Tocris Bioscience), or p38 (SB203580, 1202, Tocris Bioscience) for 1 hour prior to IL-33 stimulation (50 ng/ml). The proteins and RNAs from treated cells were collected for further analysis.

Immunoblotting. Total cellular proteins were prepared using a Triton-based lysis buffer supplemented with a proteinase inhibitor (8340, MilliporeSigma) and a phosphatase inhibitor cocktail (5870, Cell Signaling). Protein concentrations were measured, and an equal amount of protein from each sample and a size marker (26616, Thermo Scientific) were loaded onto a SDS-PAGE gel (NP0321/NP0323, Life Technologies), followed by wet-transferring onto a nitrocellulose membrane (88018, Thermo Scientific). Membranes were subsequently blocked for 30 minutes with 5% BSA (A7030, MilliporeSigma) and incubated with a specific primary antibody for 1 hour, followed by incubation for 45 minutes with a species-matched secondary antibody conjugated with IRDye. An Odyssey CLx system (LI-COR) was used for detecting positive signals. Primary and secondary antibodies are listed in Supplemental Table 1. β-Actin was used as a loading control for all blots.

qPCR. qPCR was used for quantitatively detecting gene mRNA expression. Tissues samples were homogenized in a QIAzol lysis reagent (79306, Qiagen) and were mixed with chloroform at a fixed ratio. Samples were thoroughly vortexed and centrifuged for 20 minutes. RNA-containing supernatants were collected and mixed with 100% ethanol before being subjected to an RNA extraction kit-column (K0732, Thermo Scientific). The extraction procedure was executed according to the manufacturer's instruction. For RNA preparation from culture cells, a 2-mercaptoethanol–containing lysis buffer (C3228, MilliporeSigma) was added to cells, collected, and centrifuged for 20 minutes. Total RNA concentrations were determined with a NanoDrop 2000C Spectrophotometer (Thermo Scientific), followed by cDNA synthesis using a RevertAid cDNA synthesis kit (K1632, Thermo Scientific). cDNAs were used for qPCR analysis with SYBR Green (4367659, Life Technologies) and were detected in a StepOnePlus system (Applied Biosystems). PCR was performed according to the standard recommended protocol for SYBR Green. Primers are listed in Supplemental Table 2. All data are presented as relative quantification, and GAPDH was used as an internal control.

Immunohistochemistry. PFA-fixed tumor tissues were paraffin embedded, cut into 5-μm thick sections using a microtome, and transferred onto glass slides. After baking, slides were processed through serial of steps for deparaffinization in a Tissue-Clear (1466, Sakura) system and tissues were rehydrated by stepwise-processing with 99%, 95%, and 70% ethanol. Rehydrated tissues were washed with PBS, boiled in an unmasking solution, and subsequently blocked overnight with 4% serum before incubation at 4°C with an anti-Iba1 primary antibody (rabbit, 019-19741, WAKO) or with an anti-PDGFRβ (rat, 14-1402-81, eBioscience) antibody. Slides were incubated for 30 minutes with species-specific fluorescent-conjugated secondary antibodies, including an Alexa Fluor 555–conjugated goat anti-rat (A21434, Invitrogen), an Alexa Fluor 488–conjugated donkey anti-mouse (A21202, Invitrogen), and an Alexa Fluor 488–conjugated donkey anti-rabbit (A21206, Invitrogen). For DAB staining, sections were incubated with an HRP-labeled goat anti-rat IgG as a secondary antibody (62-9520, Invitrogen). Color development was performed with 3, 3′-diaminobenzidine substrate-chromogen (DAB, SK-4100, Vector Laboratories). Hematoxylin was used for counter staining. Slides were washed and mounted with PERTEX (00801, HistoLab) or Vectashield containing DAPI (H-1200, Vector Laboratories) to allow visualization of cell nuclei. Positive signals were detected using a fluorescence microscope (Zeiss LSM510 Confocal or Nikon C1 Confocal microscopes) or a light microscope (Nikon Eclipse TS100).

Immunocytochemistry. NF-κB localization was performed on culture cells. Raw264.7 cells were seeded on coverslips and grown to 50%–70% confluency before stimulation for 1 hour with rmIL-33 (50 ng/ml) with or without prior addition of withaferin A. Cells were fixed with 4% PFA at 0-, 5-, 30-, or 60-minute intervals; permeabilized with Triton X-100 in PBS; blocked with 3% milk; and incubated

at 4°C overnight with a specific antibody against NF-κB (mouse, 6956, Cell Signaling). After washing with PBS, cells were incubated for 45 minutes at room temperature with an Alexa Fluor 488–conjugated donkey anti-mouse (A21202, Invitrogen) secondary antibody. After washing, cells were subsequently mounted with Vectashield containing DAPI (H-1200, Vector Laboratories) and stored at –20°C until analysis. Images were taken with a fluorescence microscope (Zeiss LSM510 Confocal or Nikon C1 Confocal microscopes).

H&E and Masson's trichrome. Tissue slides were deparaffinized in Tissue-Clear (1466, Sakura) and sequentially rehydrated in 99%, 95%, and 70% ethanol. For H&E, slides were stained with hematoxylin, washed thoroughly, and counterstained with eosin before dehydration with 95%–99% ethanol. For Masson's trichrome, slides were stained in a series of solutions according to the manufacturer's protocol (HT15-kit, MilliporeSigma). All slides were subsequently mounted with PERTEX (00801, HistoLab) and examined under a light microscope (Nikon Eclipse TS100).

Whole-mount staining. Fresh tumor tissues were immediately fixed at 4°C overnight with 4% PFA. Whole-mount staining was performed by cutting the tissues into small pieces, followed by digestion with a proteinase K (20 mM) Tris buffer, permeabilization with methanol, and subsequent blocking at 4°C overnight with 3% milk in Triton X-100 in PBS. Next, tissues were incubated overnight at 4°C with specific primary antibody against iBa1 (rabbit, 019-19741, WAKO), CD206 (rat, 141702, Biolegend), CD31 (rat, 553370, BD Biosciences), Laminin (rabbit, 30320, Abcam), collagen IV (rabbit, 19808, Abcam), or fibronectin (rabbit, 23750, Abcam), followed by blocking with 3% milk and incubation at room temperature for 2 hours with secondary fluorescent-conjugated antibody. Tissues were then mounted in Vectashield mounting medium (H-1000, Vector Laboratories) and stored at –20°C. A confocal microscope (Zeiss LSM510 Confocal or Nikon C1 Confocal microscopes) was used for detection of fluorescent signals and later quantified in Photoshop (CS6) software.

Affymetrix gene array and protein interaction analysis. RNA samples were prepared using the RNAeasy kit (Qiagen) and were hybridized onto Affymetrix 1.0 ST Gene arrays. Triplicates of each group were used for the gene expression analyses. Normalization and analysis for differentially expressed genes were performed using robust multiarray analysis and significance analysis of microarrays via R statistical software packages, oligo and samr. Heatmaps are presented for upregulation and downregulation of gene expression using the Multiple Experiment Viewer system (version 4.7). Gene array data were deposited in the Gene Expression Omnibus (accession GSE69402 and GSE97657).

Protein interaction analysis. The protein interaction analysis scheme was generated using an online software tool (STRING, http://www.string-db.org) using a mouse database.

Statistics. Standard 2-tailed Student's *t* test was used for all statistical analyses where $P < 0.05$ was used as a cutoff level of statistically significant results. Mean determinants are presented as ± SEM.

Study approval. All animal studies were reviewed and approved by the Stockholm North Animal Ethical Committee, Stockholm, Sweden.

Author contributions

YC designed the research and wrote the paper. PA performed most of the experiments, analyzed all raw data, prepared all figures, and helped write the Methods. YY, KH, YZ, CF, Shuzhen Liu, GY, and Shihai Liu participated in some experimentation and contributed to discussions. KH analyzed raw data and prepared figures. HB, RB, MC, and QL contributed reagents/materials; PA, YY, and YC analyzed data.

Acknowledgments

YC's laboratory is supported through the European Research Council advanced grant ANGIOFAT (project 250021), the Swedish Research Council, the Swedish Cancer Foundation, the Swedish Children's Cancer Foundation, the Karolinska Institutet Foundation, the Karolinska Institutet distinguished professor award, the Torsten Söderberg Foundation, the Maud and Birger Gustavsson Foundation, the Novo Nordisk Foundation Advance grant, and the Knut and Alice Wallenberg Foundation. YY is supported by the Natural Science Foundation of China (project 81773059) and Shanghai Pujiang Program (project 18PJ1400600).

Address correspondence to: Yihai Cao, Department of Microbiology, Tumor and Cell Biology, Karolinska Institutet, 171 77 Stockholm, Sweden. Phone: 46.8.5248.7596; Email: yihai.cao@ki.se.

1. Hanahan D, Weinberg RA. Hallmarks of cancer: the next generation. *Cell*. 2011;144(5):646–674.
2. Kalluri R. The biology and function of fibroblasts in cancer. *Nat Rev Cancer*. 2016;16(9):582–598.
3. Bardeesy N, DePinho RA. Pancreatic cancer biology and genetics. *Nat Rev Cancer*. 2002;2(12):897–909.
4. Xie D, Xie K. Pancreatic cancer stromal biology and therapy. *Genes Dis*. 2015;2(2):133–143.
5. Neesse A, et al. Stromal biology and therapy in pancreatic cancer. *Gut*. 2011;60(6):861–868.
6. Nguyen DX, Bos PD, Massagué J. Metastasis: from dissemination to organ-specific colonization. *Nat Rev Cancer*. 2009;9(4):274–284.
7. Mehlen P, Puisieux A. Metastasis: a question of life or death. *Nat Rev Cancer*. 2006;6(6):449–458.
8. Pollard JW. Tumour-educated macrophages promote tumour progression and metastasis. *Nat Rev Cancer*. 2004;4(1):71–78.
9. Condeelis J, Pollard JW. Macrophages: obligate partners for tumor cell migration, invasion, and metastasis. *Cell*. 2006;124(2):263–266.
10. Wang J, et al. Novel mechanism of macrophage-mediated metastasis revealed in a zebrafish model of tumor development. *Cancer Res*. 2015;75(2):306–315.
11. Liu C, et al. A zebrafish model discovers a novel mechanism of stromal fibroblast-mediated cancer metastasis. *Clin Cancer Res*. 2017;23(16):4769–4779.
12. Cao Y, Zhong W, Sun Y. Improvement of antiangiogenic cancer therapy by understanding the mechanisms of angiogenic factor interplay and drug resistance. *Semin Cancer Biol*. 2009;19(5):338–343.
13. Junttila MR, de Sauvage FJ. Influence of tumour micro-environment heterogeneity on therapeutic response. *Nature*. 2013;501(7467):346–354.
14. Yang Y, et al. The PDGF-BB-SOX7 axis-modulated IL-33 in pericytes and stromal cells promotes metastasis through tumour-associated macrophages. *Nat Commun*. 2016;7:11385.
15. Oboki K, et al. IL-33 is a crucial amplifier of innate rather than acquired immunity. *Proc Natl Acad Sci USA*. 2010;107(43):18581–18586.
16. Schmitz J, et al. IL-33, an interleukin-1-like cytokine that signals via the IL-1 receptor-related protein ST2 and induces T helper type 2-associated cytokines. *Immunity*. 2005;23(5):479–490.
17. Townsend MJ, Fallon PG, Matthews DJ, Jolin HE, McKenzie AN. T1/ST2-deficient mice demonstrate the importance of T1/ST2 in developing primary T helper cell type 2 responses. *J Exp Med*. 2000;191(6):1069–1076.
18. Guabiraba R, et al. IL-33 targeting attenuates intestinal mucositis and enhances effective tumor chemotherapy in mice. *Mucosal Immunol*. 2014;7(5):1079–1093.
19. Kaileh M, et al. Withaferin a strongly elicits IkappaB kinase beta hyperphosphorylation concomitant with potent inhibition of its kinase activity. *J Biol Chem*. 2007;282(7):4253–4264.
20. Chen L, Fischle W, Verdin E, Greene WC. Duration of nuclear NF-kappaB action regulated by reversible acetylation. *Science*. 2001;293(5535):1653–1657.
21. Ariyoshi W, Okinaga T, Chaweewannakorn W, Akifusa S, Nisihara T. Mechanisms involved in enhancement of matrix metalloproteinase-9 expression in macrophages by interleukin-33. *J Cell Physiol*. 2017;232(12):3481–3495.
22. Kleifeld O, et al. X-ray absorption studies of human matrix metalloproteinase-2 (MMP-2) bound to a highly selective mechanism-based inhibitor. comparison with the latent and active forms of the enzyme. *J Biol Chem*. 2001;276(20):17125–17131.
23. Umezawa K, Chaicharoenpong C. Molecular design and biological activities of NF-kappaB inhibitors. *Mol Cells*. 2002;14(2):163–167.
24. Boroujerdi A, Welser-Alves JV, Milner R. Matrix metalloproteinase-9 mediates post-hypoxic vascular pruning of cerebral blood vessels by degrading laminin and claudin-5. *Angiogenesis*. 2015;18(3):255–264.
25. Gupta GP, Massagué J. Cancer metastasis: building a framework. *Cell*. 2006;127(4):679–695.
26. Joyce JA, Pollard JW. Microenvironmental regulation of metastasis. *Nat Rev Cancer*. 2009;9(4):239–252.
27. Mantovani A, Allavena P, Sica A, Balkwill F. Cancer-related inflammation. *Nature*. 2008;454(7203):436–444.
28. Hosaka K, et al. Pericyte-fibroblast transition promotes tumor growth and metastasis. *Proc Natl Acad Sci USA*. 2016;113(38):E5618–E5627.
29. Hughes R, et al. Perivascular M2 macrophages stimulate tumor relapse after chemotherapy. *Cancer Res*. 2015;75(17):3479–3491.
30. Qian BZ, Pollard JW. Macrophage diversity enhances tumor progression and metastasis. *Cell*. 2010;141(1):39–51.
31. Dovas A, Patsialou A, Harney AS, Condeelis J, Cox D. Imaging interactions between macrophages and tumour cells that are involved in metastasis in vivo and in vitro. *J Microsc*. 2013;251(3):261–269.
32. Wyckoff J, et al. A paracrine loop between tumor cells and macrophages is required for tumor cell migration in mammary tumors. *Cancer Res*. 2004;64(19):7022–7029.
33. Hernandez L, et al. The EGF/CSF-1 paracrine invasion loop can be triggered by heregulin beta1 and CXCL12. *Cancer Res*. 2009;69(7):3221–3227.
34. Duda DG, et al. Malignant cells facilitate lung metastasis by bringing their own soil. *Proc Natl Acad Sci USA*. 2010;107(50):21677–21682.
35. Peinado H, et al. Pre-metastatic niches: organ-specific homes for metastases. *Nat Rev Cancer*. 2017;17(5):302–317.
36. Kaplan RN, et al. VEGFR1-positive haematopoietic bone marrow progenitors initiate the pre-metastatic niche. *Nature*. 2005;438(7069):820–827.
37. Hosaka K, et al. Tumour PDGF-BB expression levels determine dual effects of anti-PDGF drugs on vascular remodelling and metastasis. *Nat Commun*. 2013;4:2129.